AMERICAN SOCIETY FOR MICROBIOLOGY | Journal of Bacteriology®

RESEARCH ARTICLE

Structure of the *Streptococcus pyogenes* NAD$^+$ Glycohydrolase Translocation Domain and Its Essential Role in Toxin Binding to Oropharyngeal Keratinocytes

Jorge J. Velarde,[a] Alessandro Piai,[b] Ian J. Lichtenstein,[a] Nicola N. Lynskey,[a]* James J. Chou,[b] Michael R. Wessels[a]

[a]Division of Infectious Diseases, Boston Children's Hospital, and Department of Pediatrics, Harvard Medical School, Boston, Massachusetts, USA
[b]Department of Biological Chemistry and Molecular Pharmacology, Harvard Medical School, Boston, Massachusetts, USA

ABSTRACT The emergence and continued dominance of a *Streptococcus pyogenes* (group A *Streptococcus*, GAS) M1T1 clonal group is temporally correlated with acquisition of genomic sequences that confer high level expression of cotoxins streptolysin O (SLO) and NAD$^+$-glycohydrolase (NADase). Experimental infection models have provided evidence that both toxins are important contributors to GAS virulence. SLO is a cholesterol-dependent pore-forming toxin capable of lysing virtually all types of mammalian cells. NADase, which is composed of an N-terminal translocation domain and C-terminal glycohydrolase domain, acts as an intracellular toxin that depletes host cell energy stores. NADase is dependent on SLO for internalization into epithelial cells, but its mechanism of interaction with the cell surface and details of its translocation mechanism remain unclear. In this study we found that NADase can bind oropharyngeal epithelial cells independently of SLO. This interaction is mediated by both domains of the toxin. We determined by NMR the structure of the translocation domain to be a β-sandwich with a disordered N-terminal region. The folded region of the domain has structural homology to carbohydrate binding modules. We show that excess NADase inhibits SLO-mediated hemolysis and binding to epithelial cells *in vitro*, suggesting NADase and SLO have shared surface receptors. This effect is abrogated by disruption of a putative carbohydrate binding site on the NADase translocation domain. Our data are consistent with a model whereby interactions of the NADase glycohydrolase domain and translocation domain with SLO and the cell surface increase avidity of NADase binding and facilitate toxin-toxin and toxin-cell surface interactions.

IMPORTANCE NADase and streptolysin O (SLO) are secreted toxins important for pathogenesis of group A *Streptococcus*, the agent of strep throat and severe invasive infections. The two toxins interact in solution and mutually enhance cytotoxic activity. We now find that NADase is capable of binding to the surface of human cells independently of SLO. Structural analysis of the previously uncharacterized translocation domain of NADase suggests that it contains a carbohydrate binding module. The NADase translocation domain and SLO appear to recognize similar glycan structures on the cell surface, which may be one mechanism through which NADase enhances SLO pore-forming activity during infection. Our findings provide new insight into the NADase toxin and its functional interactions with SLO during streptococcal infection.

KEYWORDS *Streptococcus pyogenes*, NADase, toxin, NMR spectroscopy, cell binding, nuclear magnetic resonance, toxins

Streptococcus pyogenes (group A *Streptococcus* or GAS) deploys a sophisticated array of virulence factors during invasive infections. Recent evolutionary studies of the globally dominant M-type 1 (*emm1*) GAS clonal group and emerging *emm89* strains have suggested a critical role for two secreted toxins coexpressed from the same

Citation Velarde JJ, Piai A, Lichtenstein IJ, Lynskey NN, Chou JJ, Wessels MR. 2022. Structure of the *Streptococcus pyogenes* NAD$^+$ glycohydrolase translocation domain and its essential role in toxin binding to oropharyngeal keratinocytes. J Bacteriol 204: e00366-21. https://doi.org/10.1128/JB.00366-21.

Editor Michael J. Federle, University of Illinois at Chicago

Address correspondence to Jorge J. Velarde, Jorge.Velarde@childrens.harvard.edu, or Michael R. Wessels, Michael.Wessels@childrens.harvard.edu.

*Present address: Nicola N. Lynskey, The Roslin Institute, University of Edinburgh, Edinburgh, UK.

Received 13 July 2021
Accepted 18 October 2021
Accepted manuscript posted online 25 October 2021
Published 18 January 2022

operon, streptolysin O (SLO) and NAD^+-glycohydrolase (NADase) (1, 2). Genome analysis of 3,615 *emm1* GAS clinical isolates collected over more than 40 years found that a key event temporally associated with the emergence of the currently dominant *emm1* strain was recombination of a 36-kb region of the GAS chromosome that includes the *nga/slo* operon encoding NADase and SLO (1, 3). This recombination event introduced polymorphisms in the promoter that increased expression of both toxins as well as amino acid substitutions in NADase that increased its enzymatic activity (2, 3). Similar polymorphisms have been identified in invasive *emm89* strains emerging in several countries around the world (4, 5). Furthermore, deletion of NADase, SLO, or both toxins decreases virulence in animal models of invasive infection. Zhu et al. found significant attenuation of virulence of isogenic mutants harboring deletions of either toxin independently or of the entire operon in mouse bacteremia, myositis, and subcutaneous infection models (6).

SLO is a member of the cholesterol-dependent cytolysin family of toxins (7, 8). It binds to host cells, oligomerizes, and inserts in the plasma membrane to form large pores that result in lysis of most cell types including immune and epithelial cells. The enzymatic function of NADase is to cleave NAD, and translocation of NADase into host cells promotes cell death through degradation of intracellular NAD and depletion of cellular energy stores (9–12). In combination with SLO, NADase enhances intracellular survival of GAS in epithelial cells and professional phagocytes (13, 14). The two toxins have an intimate relationship during pathogenesis in that interaction between NADase and SLO after secretion from the bacterium is important for stability of both proteins in solution (15). Subsequently, NADase requires the presence of SLO for translocation into the host cell cytoplasm, a process termed cytolysin-mediated translocation (CMT) (16). Although it was initially thought that NADase was introduced into the host cell through the SLO pore, subsequent work suggests that pore formation is not necessary for NADase translocation (17).

NADase consists of two distinct domains. The N-terminal ~194 amino acids encompass a signal sequence (residues 1 to 37) and the translocation domain. Even small deletions in this region decrease the amount of toxin translocated into the host-cell cytoplasm in an *in vitro* infection model (18). The remainder of the protein comprises the glycohydrolase domain, which is responsible for cleavage of NAD to nicotinamide and ADP-ribose. The crystal structure of this domain has been solved (19, 20). However, attempts to crystallize the entire toxin were unsuccessful. Modeling of the translocation domain predicts it contains a glycan-binding domain (21). However, its structure has not been experimentally determined. Mozola et al. also demonstrated that NADase can alter the mechanism by which SLO binds to cells (21). These findings suggest the possibility of an independent receptor for NADase although direct binding of NADase to cells has not yet been demonstrated. Thus, the mechanism by which NADase associates with epithelial cells and enters the cytoplasm remains incompletely characterized.

In this study, we further investigated the interaction between NADase and oropharyngeal epithelial cells. We show that purified NADase directly interacts with the surface of oropharyngeal keratinocytes (OKP7), and that the translocation domain contributes to cell binding. We subsequently determine by solution NMR the structure of the NADase translocation domain to be a β-sandwich with structural homology to bacterial carbohydrate binding modules (CBMs) and an extended N-terminal largely disordered region. Finally, we provide evidence that both NADase and SLO may interact with similar cell surface structures. Our results provide new insight into how NADase contributes to GAS pathogenesis by direct interaction with host cells and its cotoxin SLO.

RESULTS

NADase binds to the surface of oropharyngeal keratinocytes in the absence of SLO. Our laboratory has previously purified full-length NADase as well as recombinant peptides corresponding to its translocation and glycohydrolase domains, both of

which contribute to NADase binding to SLO (15). Although SLO is necessary for translocation of NADase to the host cell cytoplasm, *in vitro* infection data suggest NADase may bind to the host cell independently (21, 22). To investigate whether purified NADase can bind to oropharyngeal keratinocytes (OKP7), we incubated OKP7 cells with Alexa Fluor 488-labeled NADase or ovalbumin as a negative control. After 30 min of incubation at 37°C, cells were washed, fixed, and analyzed by flow cytometry (Fig. 1A and B). Mean fluorescence intensities (MFI) were significantly greater for cells treated with NADase (MFI 35.0) compared to cells treated with either phosphate-buffered saline (PBS) (5.1) or ovalbumin (11.9) ($P < 0.001$). These data suggest that NADase binds to oropharyngeal epithelial cells even in the absence of SLO. We performed similar experiments with Alexa Fluor 488-labeled peptides corresponding to the N-terminal translocation domain (residues 38 to 194, NT194) or the C-terminal glycohydrolase domain (residues 190 to 451). Binding of both constructs was reduced compared to the full-length toxin (Fig. 1) ($P < 0.01$).

As a complementary approach to flow cytometry, we used fluorescence microscopy to visualize NADase binding to OKP7 cells attached to a glass cover slip. Representative images show distinct punctate regions of NADase bound to the periphery of fixed keratinocytes (Fig. 1C and D). In contrast, we saw little to no fluorescence for the glycohydrolase domain alone or for the IFS negative control. IFS is an inhibitor of NADase, which is encoded in the same operon, but is not secreted from the bacterium. We did not expect IFS to bind to cells and included it as a negative control. The percentage of cells with visible bound toxin was quantified from three independent experiments (Fig. 1D). The results are consistent with flow cytometry data in that the greatest binding was observed for the full-length toxin.

These results imply that both domains are necessary for maximal binding of NADase to oropharyngeal keratinocytes.

The structure of the NADase translocation domain is a β-sandwich with structural homology to bacterial carbohydrate binding modules and it is preceded by a disordered region. Although the crystal structure for the NADase C-terminal glycohydrolase domain has been solved, no experimentally determined structure is available for the N-terminal translocation domain. We recently demonstrated that this domain is important for NADase binding to SLO (15). The results above show that the translocation domain contributes to toxin association with epithelial cells. To better understand how NADase interacts with its cotoxin SLO and with host cells, we used solution NMR to solve the structure of the NADase translocation domain. Residue numbering in this study was based on wild-type full-length NADase. Amino acids 1 to 37 correspond to the signal sequence. The mature translocation domain starts at V38, and our construct extended to residue N194 (157 total amino acids). G36 and P37 of our construct are cloning and purification artifacts. We were able to assign 91% of 154 nonproline amide backbone chemical shifts. A two-dimensional ^{1}H-^{15}N TROSY-HSQC spectrum is included in the (Fig. S1 in the supplemental material). The solution structure of the translocation domain (Fig. 2A and S2) has seven β-strands arranged into a β-sandwich with two opposing antiparallel sheets. β-Strands are comprised of the following amino acids: β1, V93 to K97; β2, R106 to V110; β3, K128 to Y134; β4, V140 to E146; β5, H156 to E159; β6, R168 to V173; and β7, V190 to G193 The translocation domain also contains a single small α-helix composed of residues K117 to K122 between β2 and β3 (Fig. 2B). Finally, the N-terminal region of the translocation domain, from V38 to ~S78, exhibits the characteristic features of an intrinisically disordered region (IDR) (23). Further chemical shift analyses of this region based on the model-free order parameter RCI-S^2 (24, 25) and neighbor corrected structural propensity (ncSP; https://pubs.acs.org/doi/10.1021/ja105656t) indicate that the disordered region is not completely flexible but instead transiently adopts local secondary structure elements, which may be stabilized upon interactions with SLO or another ligand (Fig. 2C and D).

Previous structural prediction of the NADase translocation domain was based on sequence homology to CBMs (21). We used the experimentally determined NMR structure of the translocation domain to further investigate structural homologies. The

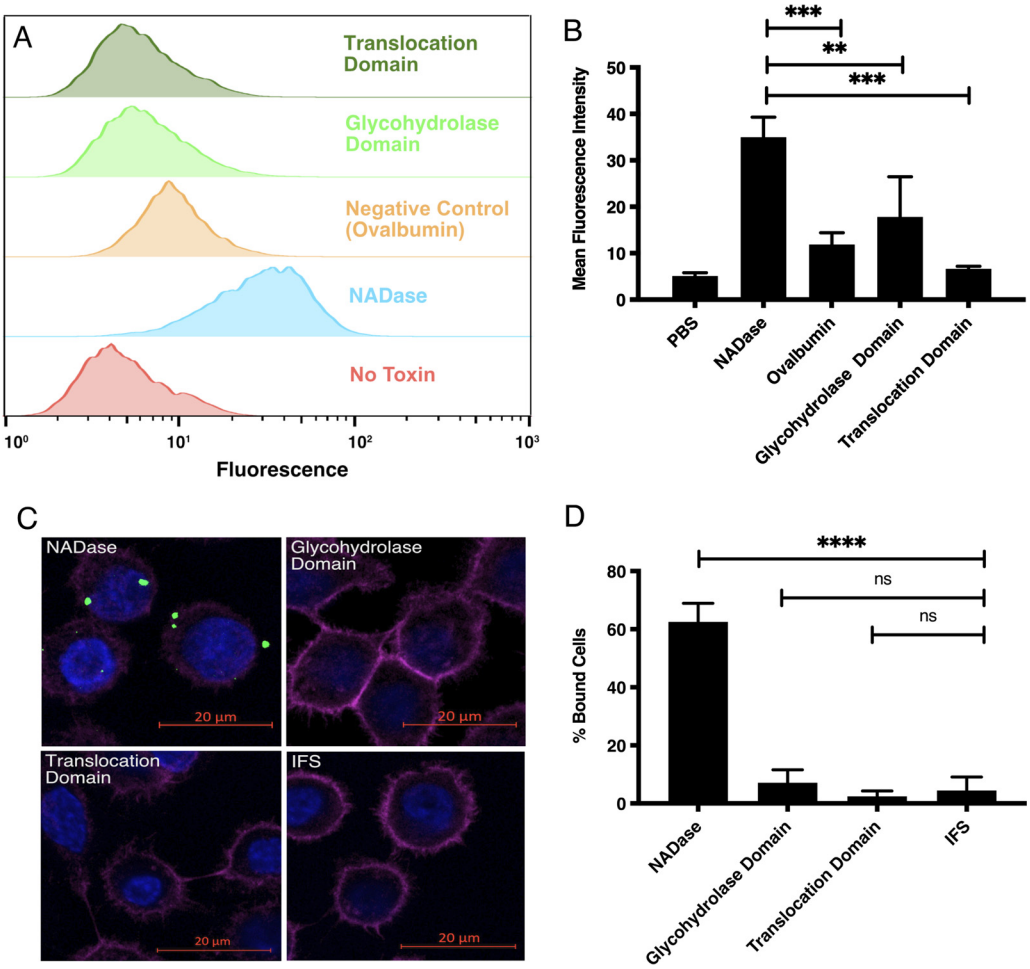

FIG 1 NADase can bind to the surface of oropharyngeal keratinocytes in the absence of SLO. (A) Representative flow cytometry data. Directly labeled NADase (Alexa Fluor 488) or its purified domains were bound to keratinocytes in suspension. Cells were washed, fixed, and analyzed by flow cytometry. (B) Mean fluorescence intensity average of 3 independent experiments. Binding of NADase is significantly increased compared to an ovalbumin negative control, the isolated NADase translocation domain, and the isolated glycohydrolase domain. (C) Confocal microscopy of NADase constructs bound to oropharyngeal keratinocytes. Representative images of labeled toxin, in green, bound to OKP7 cells. Cells were additionally stained with DAPI (blue) and phalloidin (magenta). (D) Quantitation of percent of total cells with bound toxin. A total of >100 cells were counted by an observer blinded to the treatment condition. NADase binding was significantly increased compared to its fragments or IFS. Statistical significance was detemined by ANOVA with Tukey's posttest (****, $P < 0.0001$; ***, $P < 0.001$; **, $P < 0.01$).

closest homologs based on a DALI (26) search of the Protein Data Bank (PDB) (Fig. 3A and B; Table 1) were family 32 CBMs (CBM32). They include a putative CBM from EndoD of *Streptococcus pneumoniae* (27) and a CBM from a *Clostridium perfringens* glycoside hydrolase (28). We also queried whether there was any structural homology with the lectin domain of lectinolysin, a cytolysin secreted by *Streptococcus mitis* (29). A DALI-based comparison of the structured region of the NADase translocation domain yielded an alignment to lectinolysin with a Z-score of 5.9 and root-mean-square deviation (RMSD) of 3.3 Å (Fig. 3C; Table 1). CBMs can be associated with a calcium ion that contributes to the overall structure. However, investigation of the effects of calcium on the NADase translocation domain both by microcalorimetry and chemical shift perturbation experiments of an ^{1}H-^{15}N TROSY-HSQC spectrum (Fig. S3 in the supplemental material) did not reveal interactions with calcium. Glycan binding by CBM32 family members typically requires both aromatic side chains that participate in Π-stacking interactions with carbohydrate rings and polar residues that form hydrogen bonds with the sugar (30). An electrostatic potential map of the structure demonstrated an

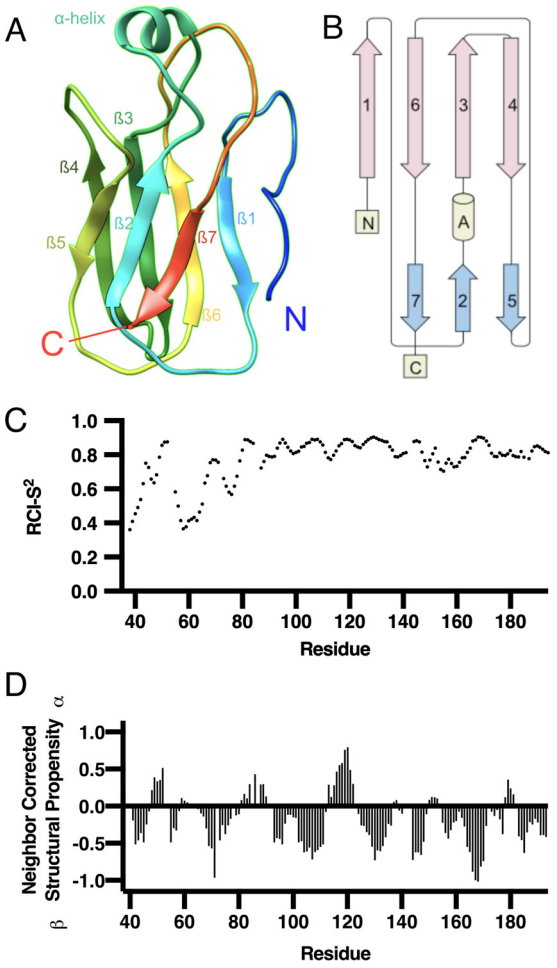

FIG 2 NADase translocation domain solution structure. The solution structure of the NADase translocation domain contains a β-sandwich with a short α-helix at one end and an N-terminal disordered region. (A) Ribbon representation of amino acids 76–194. B. Secondary structure topological schematic diagram shows 2 antiparallel β-sheets and an α-helix. (C) Random coil index-based (RCI) order parameters (S^2), which are calculated with experimentally determined chemical shifts (^{15}N, $^{13}C^{\alpha}$, $^{13}C^{\beta}$, $^{13}C'$). The lower values at the N-terminus suggest increased disorder consistent with our NOE data. (D) Neighbor corrected structural propensity scores calculated using experimentally determined chemical shifts. A positive value denotes propensity for α-helix. A negative value denotes propensity for β-strand. Residues 42 to 46, 55 to 57, and 67 to 80 exhibit a propensity for β-strand; and residues 49 to 52 exhibit a propensity for α-helix. This suggests they may adopt some secondary structure when interacting with SLO or a ligand.

abundance of polar, positively charged residues (Fig. 3D) in the region predicted, based on structural homologies discussed above, to mediate glycan binding. Similarly, multiple solvent-exposed aromatic side chains could be identified (Fig. 3E). These observations imply that the NADase translocation domain likely interacts with glycans.

High concentrations of NADase impede cell surface binding of SLO. NADase was previously shown to affect host cell binding of SLO in an *in vitro* infection model (21). We wondered whether the presence of NADase would similarly affect SLO binding to OKP7 cells *in vitro* using purified toxins. We used SLO with G395V and G396V amino acid substitutions, which lock the toxin in a monomer conformation (m-SLO) (17). These amino acid substitutions eliminated oligomerization and pore formation as confounders in the assay. Based on the previously reported K_D of interaction between SLO and NADase, we tested cell binding of Alexa Fluor 488-labeled m-SLO at 20 nM in solution with unlabeled full-length NADase at 10 μM. Toxins were incubated with OKP7 cells at 37°C for 20 min, and then the cells were washed, fixed and assayed for fluorescence by flow cytometry (Fig. 4). Fluorescence in these experiments is representative

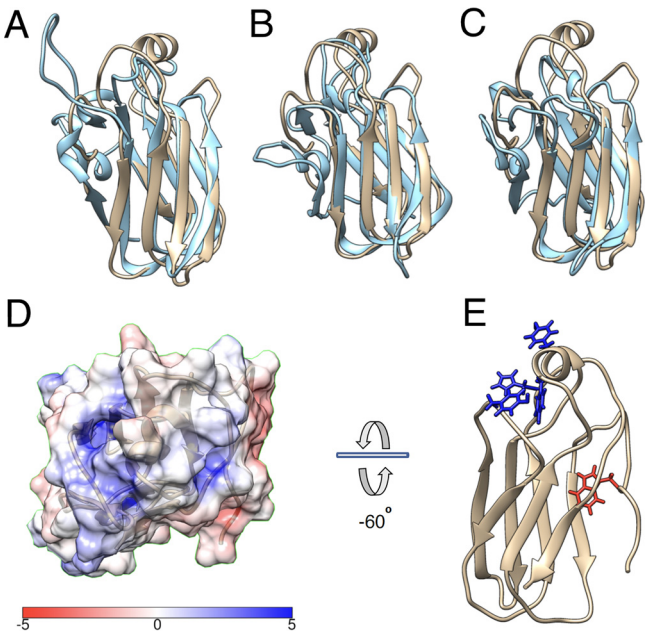

FIG 3 Structural comparison and analysis of NADase translocation domain. Pictured are alignments of the NADase translocation domain (tan) with three carbohydrate binding domains (blue) identified from a DALI search: CpGH31 CBM32-2 (PDB ID 4uap) from *Clostridium perfringens* (A); CBM32 of EndoD (PDB ID 2xqx) from *Streptococcus pneumoniae* (B); lectin domain of lectinolysin (PDB ID 3le0) from *Streptococcus mitis*. (D) Electrostatic potential of the NADase translocation domain focusing on region predicted to bind possible glycan. Surface potential values are in kT/e. E. Aromatic residues in predicted glycan binding domain (Y120, Y121, Y151, H177). W81, previously predicted to participate in glycan binding, is depicted in red.

of m-SLO binding to cells. We noted a robust fluorescent signal from cells exposed to m-SLO alone (MFI 220.0). However, binding of m-SLO was significantly inhibited in the presence NADase (MFI 46.73), an effect that was not seen for m-SLO and 10 μM IFS (MFI 290.7) used as a negative control. Thus, a high concentration of NADase inhibits m-SLO binding to the surface of oropharyngeal keratinocytes *in vitro*.

Substitutions to aromatic amino acids at the putative glycan binding site of the translocation domain abrogate the cell-binding inhibitory effects of NADase on SLO. SLO must interact with surface glycans for proper function and has high affinity for carbohydrate structures with terminal galactose (31). Because of its homology to CBMs, we wondered whether NADase might compete with SLO for cell surface glycans, thereby inhibiting m-SLO binding to OKP7s as observed above. We thus hypothesized that substitutions to aromatic amino acids predicted to be at the putative glycan binding site of the NADase translocation domain (Fig. 3E) would alter the inhibitory effect of high concentrations of NADase on m-SLO cell surface interactions. We purified full-length NADase with tyrosine to alanine substitutions at amino acid 151 (NADase Y151A) and also at amino acids 120 and 121 (NADase Y120A,Y121A). As a mutagenesis control, we additionally substituted H103 (NADase H103A) which is on the opposite pole of the β-sandwich from the predicted site of glycan interaction. We then tested the ability of the mutant NADase constructs to inhibit binding of Alexa Fluor 488 labeled m-SLO to OKP7 cells as assessed by flow cytometry (Fig. 5A). We found significantly reduced inhibition of

TABLE 1 Homology statistics for 3 carbohydrate binding modules depicted in Fig. 3 and identified by DALI structural homology search

Protein (PDB ID)	Species	Z-score	RMSD (Å)	% identity of structurally equivalent residues
CpGH31 CBM32-2 (4uap)	*Clostridium perfringens*	7.3	3.5	16
EndoD, SpCBM32 (2xqx)	*Streptococcus pneumoniae*	7.3	3.1	11
Lectinolysin, lectin domain (3le0)	*Streptococcus mitis*	5.9	3.3	15

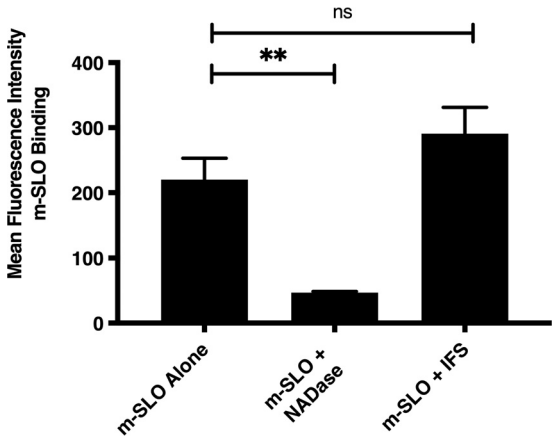

FIG 4 NADase inhibits m-SLO binding to keratinocytes. Alexa Fluor 488-labeled m-SLO was added to OKP7s in suspension either alone or with 10 μM NADase. Cells were then washed, fixed, and analyzed by flow cytometry. Fluorescence under all conditions represents binding of m-SLO to cells which is inhibited by excess NADase. Data were analyzed from three independent experiments by ANOVA with Tukey's posttest (**, $P < 0.01$).

m-SLO binding by NADase Y151A (MFI 91.00) and NADase Y120A,Y121A (MFI 163.0) compared with wild-type NADase (MFI 46.73) or the mutagenesis control NADase H103A (MFI 32.97). Thus, the tyrosine substitutions at the putative carbohydrate binding site of the NADase translocation domain abrogated the inhibitory effect of excess NADase on m-SLO cell surface interactions. We further tested this effect on SLO binding to and lysis of red blood cells (Fig. 5B) and found that NADase could inhibit the hemolytic effect of 0.5 nM SLO with an IC_{50} of 1.64 μM. NADase H103A had a similar IC_{50} of 1.35μM. However, NADase Y151A exhibited a signficantly increased IC_{50} of 4.63 μM ($P = 0.0018$ versus NADase). We were unable to reach an IC_{50} for NADase Y120A,Y121A with concentrations up to 20 μM. IFS as a negative control at the same concentrations as the NADase constructs had no effect on SLO-mediated hemolysis. Circular dichroism (CD) spectroscopy of purified NADase Y151A and NADase Y120A,Y121A compared with wild-type NADase demonstrated changes in CD spectra consistent with tyrosine substitutions but not suggestive of disruption of secondary structure of the NADase toxin (Fig. 5C). The overall folded state of the toxin constructs was also confirmed by dynamic light scattering which demonstrated similar hydrodynamic radii for the NADase wild-type and mutant constructs (Table 2). We considered the possibility that high concentrations of NADase sequester SLO from binding to the cell surface. If so, we would expect a decreased binding affinity between m-SLO and NADase Y151A or NADase Y120A,Y121A, compared with wild-type NADase, thereby freeing m-SLO for cell surface binding. We determined dissociation constants for interactions of the mutant NADase constructs with m-SLO by biolayer interferometry (BLI) as previously described (15). These experiments found no significant difference in binding affinity between the toxins (Table 2). Although substitutions to tyrosine residues at the putative glycan binding site of the NADase translocation domain do not affect secondary structure nor binding affinity to SLO, they clearly abrogate the *in vitro* inhibitory effect of an overabundance of NADase on SLO binding to the cell surface. Fluorescence microscopy to directly determine changes in epithelial cell interactions of NADase Y120A,Y121A and NADase Y151A was not sensitive enough to demonstrate differences, consistent with a multivalent interaction on the cell membrane rather than a 1:1 glycan receptor interaction. Nevertheless, competition for cell surface binding in our experiments suggests that both NADase and SLO can bind to similar glycan structures on the cell surface.

DISCUSSION

Studies of evolutionary changes that facilitated emergence of the globally dominant GAS *emm1* clonal group and newly emerging *emm89* strains have implicated

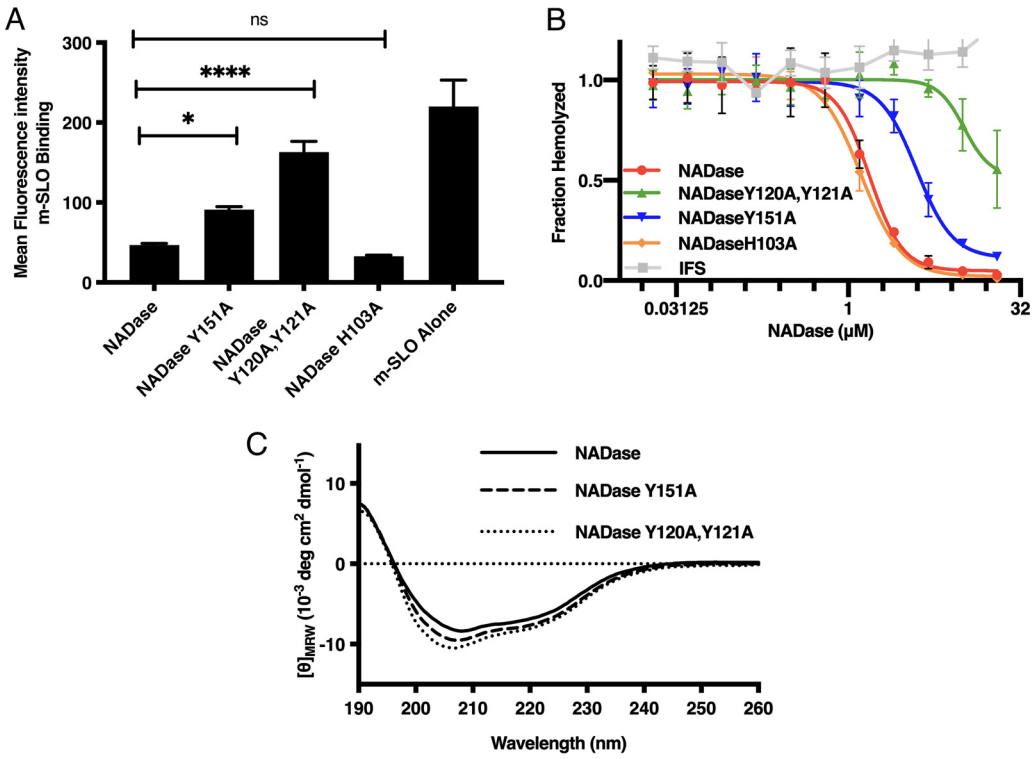

FIG 5 Aromatic amino acid substitutions of the NADase translocation domain abrogate the inhibitory effect of NADase on m-SLO cell binding. (A) The inhibitory effect of excess wild-type full-length NADase (10 μM) on cell binding of m-SLO (20 nM) was abrogated by a Y151A substitution and Y120A and Y121A substitutions but not an H103A substitution (negative control). (B) Similarly, NADase inhibited hemolysis by wild-type SLO (0.5 nM) with an IC_{50} of 1.64 μM. This effect was decreased for the NADase variants except for H103A. (C) Spectral variation of circular dichrosim analysis was consistent with NADase tyrosine substitutions but not with disruption of secondary structure or overall architecture of the toxin. Statistical analysis from at least three independent experiments was completed with GraphPad Prism 9.0 using ANOVA with Tukey's comparison. (*, $P < 0.05$; ****, $P < 0.0001$).

polymorphisms in the promoter of the *nga/slo* operon resulting in increased expression of NADase and its co-toxin SLO (2). Animal models of pathogenesis also support the importance in virulence of each toxin (6). NADase and SLO interact upon secretion from the bacterium and presumably approach the host-cell membrane as a heterodimer (15). SLO binds to cholesterol in the cell membrane and may utilize cell surface glycans as additional receptors. Yet, physical association of SLO with the cell surface can be modified or augmented by its interactions with NADase. Shewell et al. demonstrated that SLO bound several glycans with the highest affinity for lacto-*N*-neotetraose (LNnT) and that exogenous LNnT could inhibit SLO-mediated hemolysis, suggesting that binding to a glycan was necessary for SLO pore formation on red blood cells (31). Mozola et al. subsequently showed that in strains harboring mutations of the SLO carbohydrate binding site, NADase expression augmented SLO-mediated pore formation in target cells (21). The authors suggested that NADase may bind to cells in association with SLO and provide an alternative mechanism by which nonglycan-binding SLO can

TABLE 2 Biophysical characteristics of NADase and NADase variants[a]

NADase variant	Hydrodynamic radius (nm)	Biolayer interferometry K_D (95% CI)
NADase	3.89 ± 0.67	12.18 μM (9.70–15.41)
NADaseH103A	3.96 ± 0.72	9.37 μM (7.41–11.91)
NADaseY151A	4.51 ± 0.52	8.00 μM (6.49–9.88)
NADaseY120A,Y121A	5.23 ± 0.97	6.22 μM (4.57–8.47)

[a]Hydrodynamic radius was determined by dynamic light scattering. K_D for the interaction between m-SLO with NADase or NADase variants was determined by biolayer interferometry.

interact with the cell membrane. Finally, NADase depends on SLO for translocation into the host-cell cytoplasm by CMT, a process that is independent of SLO pore formation (16, 17). Fundamental questions, however, remain unanswered regarding the interaction of NADase and SLO with epithelial cells. Until now, it has been unclear whether NADase is capable of binding to the cell surface independently of SLO.

In this study, we examined the ability of NADase to bind oropharyngeal epithelial cells. We found that purified full-length NADase is capable of interacting with oropharyngeal keratinocytes, and that this interaction is dependent on both an N-terminal translocation domain and a C-terminal glycohydrolase domain of the toxin. These data are consistent with published results showing that both domains of the NADase toxin are needed for CMT (18), which must be preceded by toxin binding to targeted cells. The effects on translocation from deletion of either domain may, in part, be a result of decreased NADase binding.

An NADase receptor has not yet been identified. However, Mozola et al. have suggested a possible glycan receptor based on sequence homology with CBMs (21). We were able to experimentally determine the solution structure of the NADase translocation domain. A DALI structural homology search identified CBM32 family members, which are type C topology CBMs (30). Our analysis of the NMR structure identified several conserved features consistent with a CBM. The most common structural motif in this family of proteins is the β-sandwich; NADase has four-stranded and three-stranded ß sheets arranged into a sandwich configuration. The location of glycan binding for CBM32 members and other class C topology glycan binding modules is at the edge of the characteristic β-sandwich. Critical residues for substrate recognition include aromatic side chains, largely tryptophan and tyrosine, that form stacking interactions with sugar rings of their ligands. In addition, polar residues are important for hydrogen bonding interactions and increase affinity to their cognate carbohydrates (30). The NADase translocation domain has several readily identifiable aromatic residues (Y120, Y121, Y151, and H177) at one end of the β-sandwich domain. Further examination of electrostatic potentials identified proximal basic regions that could participate in hydrogen bonding for substrate recognition. Previous mutagenesis data have implicated tryptophan 81 for potential glycan binding (21). Substitution of tryptophan 81 with alanine in a strain harboring an otherwise intact *slo/nga* operon reduced NADase association with the membrane fraction of CHO cells and abrogated CMT of the mutant toxin. Whether this substitution resulted in any change to the overall protein structure was not reported. In our NMR experiments, we observed nuclear Overhauser effects (NOEs) between the aromatic ring of W81 and hydrophobic residues of β1, β6, and β7, representative of interactions with hydrophobic side chains from residues in these strands (L94, I171, L187, and V190). These interactions render the tryptophan side chain in our structure unavailable for glycan binding. Disruption of these interactions could have an effect on the architecture or stability of the translocation domain and its interactions with the cell, SLO, or both. Alternatively, it is possible that under different conditions, in the full-length NADase toxin, or in the presence of SLO, the region containing W81 does not exhibit these intramolecular interactions and the aromatic side chain of W81 may become available for carbohydrate recognition.

An aspect of the solution structure which differs from the structural homologs identified is the extended N-terminal disordered region of the translocation domain. Analysis of its structural propensity based on experimentally determined chemical shifts suggests that the region samples transient secondary structures and may participate in the architecture of the globular domain under different conditions, potentially in the presence of full-length NADase or SLO. However, these preformed structure elements may also become stabilized upon interaction with the membrane or other ligand(s), an effect that has been described for intrinisically disordered proteins (IDPs) and regions (IDRs) (23).

Based on the observations of Mozola et al. (21) showing enhancement of SLO binding by NADase in an infection model, we initially hypothesized that high concentrations of NADase above the K_D for the interaction of the two toxins, allowing them to interact in an *in vitro* model, would result in enhanced SLO cell surface interactions. However, a binding

assay of m-SLO at nM concentrations and NADase at almost 3-log higher concentrations instead resulted in inhibition of m-SLO binding to epithelial cells and inhibition of wild-type SLO-mediated hemolysis. We considered whether interactions with NADase might instead sequester SLO from interactions with the cell. Such a model would be inconsistent with previous data suggesting the toxins associate in solution and may approach the membrane as heterodimers (15, 21, 22). Nevertheless, we reasoned that if this hypothesis were true, our amino acid substitutions of the translocation domain in full-length NADase (NADase Y151A and NADase Y120A,Y121A) which abrogate the inhibitory effect on SLO without disrupting the overall structure of NADase should exhibit lower affinity binding to m-SLO. However, as determined by BLI, their K_D was not significantly different from that of wild type NADase. We subsequently concluded that high concentrations of NADase therefore compete with SLO for similar structures on the cell surface. Decreased inhibition by NADase Y120A,Y121A and NADase Y151A implicate the substituted tyrosine residues in the observed effect and are highly suggestive of oligosaccharide interactions on the cell surface. The two toxins are not likely to compete for abundant cell surface glycans during natural infection where they approach the membrane as a 1:1 heterodimer (15). However, our *in vitro* competition data suggest that both toxins bind similar oligosaccharides. As suggested by Mozola et al., interactions with SLO may therefore enhance cell binding of NADase *in vivo* (21). The cumulative effect of a multidomain NADase and SLO heterodimer binding to similar glycans may be to increase the avidity of NADase, overall interaction with the cell surface, and subsequent translocation.

Lectinolysin from *Streptococcus mitis* is a cytolysin that harbors a lectin domain which augments pore forming activity on platelets, although the same effect is not seen for hemolysis (32, 33). This is presumably mediated by clustering of the toxin (29, 32). As the translocation domain of NADase has significant structural homology with the lectin domain of LLY (Fig. 3), it is plausible that binding to cell surface glycans could cluster NADase molecules by a similar mechanism. We also note that the N-terminal domain of the NADase disordered region is largely positively charged. Electrostatic interactions of this region, as often found in other IDPs (34), could be directed at negative charges on the extracellular surface of the plasma membrane. Based on our observations, a potential model for the demonstrated synergystic effect of NADase on SLO pore formation and killing (15) is one in which interactions of SLO, along with the structured and disordered regions of the NADase translocation domain, with surface oligosaccharides help cluster the toxins and recruit, for instance, glycosphingolipids on the cell surface. Cholesterol is known to be associated with the ceramide portion of glycosphingolipids; local enrichment with ceramides augments cholesterol access by cholesterol-dependent SLO thereby increasing its lytic activity (35, 36). The net effect would thus be enhanced activity of streptolysin O.

In summary, we find that NADase can bind to oropharyngeal keratinocytes independently of its cotoxin SLO. This interaction is dependent on the NADase glycohydrolase domain and the translocation domain, which is homologous to CBMs. At high concentrations, NADase competes with SLO for carbohydrate interactions on the cell surface. NADase may therefore bind similar surface glycans as SLO, and at physiologic concentrations, through interactions between the two toxins, NADase may enhance clustering and activity of this critical cytolysin.

MATERIALS AND METHODS

Bacterial strains and growth conditions. *E. coli* NEB5α (New England Biolabs) were used for plasmid manipulation and BL21 (New England Biolabs) were used for all protein expression. *E. coli* were grown in Luria-Bertani broth at 37°C unless otherwise indicated. When necessary, antibiotics were added for *E. coli* at the following concentrations: carbenicillin at 100 μg/ml, ampicillin at 100 μg/ml, and kanamycin at 50 μg/ml.

DNA and plasmid manipulation. Plasmids for expression of NADase Y151A (pET*nga_ifs*_y151a), NADase H103A (pET*nga_ifs*_h103a), and NADase Y120A,Y121A (pET*nga_ifs*_y120a_y121a) were constructed from pET*nga_ifs* (15, 37). Primers are listed in Table S2 in the supplemental material and were used for QuikChange site directed mutagenesis per the manufacturer's recommendations (Agilent Technologies Inc., CA).

The plasmid for expression of m-SLO was constructed again by QuikChange mutagenesis described

above with primers as described in Table S2 in the supplemental material and template pETslo (15). The resulting plasmid was named pETslo_g395v_g396v.

All constructs were sequenced to confirm fidelity of cloning and mutagenesis.

Protein expression, purification, and labeling. Full-length NADase was expressed in BL21 at 30°C for 3 to 3.5 h. Toxin was then purified as previously described (37) omitting the anion exchange step. Protein was exchanged into PBS or Tris300 buffer (20 mM Tris, 300 mM NaCl, pH 8.0) with 1 mM dithiothreitol (DTT), during gel filtration or by dialysis after purification. NADase constructs with amino acid substitutions were expressed and purified exactly as described for wild-type full-length NADase.

Initial expression and purification of the NADase translocation domain (NT194) was as previously described (15) with few modifications. Expression was done at 30°C for 3 to 5 h. After initial protocol referenced above, we concentrated protein in Vivaspin concentrators (GE Healthcare) and then further purified it on a Superdex 75 10/300GL column in Tris300.

Monomeric SLO was purified from expression vector pETslo_g395v_g396v as previously described for wild-type SLO (15).

NADase NT194 labeled with stable isotopes was expressed in minimal medium supplemented with ^{15}N-NH_4Cl, ^{13}C-glucose, or both at 30°C for 5 h after reaching exponential growth. Triple-labeled samples were expressed in 99% D_2O supplemented with ^{15}N-NH_4Cl and ^{13}C-glucose, after passaging in minimal medium with 70% and 90% D_2O. Once cultures reached mid-logarithmic phase in medium with 99% D_2O, they were induced with 0.8 mM IPTG at 30°C and allowed to express for 10 h. NMR samples were purified as described for unlabeled samples and either buffer exchanged during gel filtration or dialyzed after purification into NMR buffer (20 mM MES, 50 mM NaCl, pH 5.5).

IFS and the NADase glycohydrolase domain (190NADase) were purified as previously described (37). Ovalbumin was purchased already pure (GE HEalthcare).

Toxin constructs were labeled with Alexa Fluor 488 for both flow cytometry and fluorescence microscopy. Alexa Fluor 488 NHS ester (Thermo) was added to protein in PBS per manufacturer instructions at room temperature for 1 h. The reaction was then quenched with 100 mM Tris (pH 8.0) and the protein was exchanged over a 2 ml Zeba spin column (Thermo) into Tris300 buffer with 1 mM DTT. The material was then dialyzed extensively into the same buffer to remove any remaining free dye. Molar ratios of dye to protein were determined with A_{280} and A_{495} measurements per manufacturer recommendations. m-SLO was biotinylated with EZ-Link sulfo-NHS-LC-LC-biotin per the manufacturer's instructions (Thermo). The reaction was carried out in PBS for 30 to 45 min at room temperature and then quenched with 100 mM Tris (pH 8.0). m-SLO was then dialyzed into 20 mM Tris, 300 mM NaCl, 1 mM DTT, 0.01% Tween, pH 7.4. Reaction efficiency was assayed with the Pierce biotin quantitation kit (Thermo).

NMR spectroscopy and structure determination. NMR samples were in 20 mM MES, 50 to 80 mM NaCl, with or without 0.5 mM EDTA (pH 5.5), 10% D_2O, and all experiments were at 303 K. The presence or absence of EDTA did not alter NMR spectra (Fig. S4 in the supplemental material). Sequence specific backbone assignment was completed using a standard suite of triple resonance experiments (38, 39) using ^{15}N-^{13}C- and 85% ^{2}H labeled ~500 to 750 μM NADaseNT194 on a Bruker Avance III HD spectrometer operating at 600 MHz ^{1}H frequency equipped with a cryoprobe. Experiments included TROSY versions of the two-dimensional (2D) ^{1}H-^{15}N HSQC, 3D HNCA, 3D HNCACB, 3D HN(CA)CO, 3D HNCO, and 3D HN(CO)CA. Side chain assignment and distance restrains were achieved acquiring a 3D ^{15}N-edited NOESY-TROSY-HSQC (mixing time, 80 ms) and a 3D ^{13}C-edited NOESY (mixing time, 150 ms) spectra along with the lower-dimensionality corresponding 2D ^{1}H-^{15}N TROSY-HSQC and 2D ^{1}H-^{13}C HSQC spectra using protein concentrations of 1 mM on a Bruker Avance III spectrometer operating at 800 MHz ^{1}H frequency equipped with a cryoprobe. NMR data were processed in NMRPipe (40). Spectral analyses were completed in CARA (41), Xeasy (42), and Sparky (T. D. Goddard and D. G. Kneller, SPARKY 3, University of California, San Francisco). TALOS+ (24) was used for prediction of dihedral angles using available chemical shift assignments. Secondary structure was determined using TALOS-based chemical shift indexing and validated by inspection of short- and long-range NOE data. Structure calculation was performed by simulated annealing (SA) using XPLOR-NIH (43). A combination of NOE distance restraints, dihedral restraints from TALOS+, and hydrogen bonding restraints based on determined secondary structure were used for structure calculation. The simulated annealing bath was cooled from 1,000 K to 200 K with 20 steps. Simulated annealing structure calculations included 215 long-range NOEs, 294 short-range NOEs, 158 dihedral angle restraints, and 50 hydrogen bonding restraints. One-hundred fifty structures were calculated, and the 15 structures with the lowest energy displayed a backbone RMSD from their average of 1.083 $\pm$ 0.145 Å and 1.896 $\pm$ 0.154 Å for all heavy atoms (Table S1 in the supplemental material). Structure quality determination was completed with MOLPROBITY (44) and PROCHECK (45) (Table S1). Structures were visualized and rendered with PyMOL (46) and Chimera (47). Surface electrostatic potentials were calculated with the Delphi web server (48, 49) and structural homologies were determined and calculated on the DALI server (50). The secondary structure schematic was drawn with Pro-origami (51). RCI-S^2 were calculated using TALOS (24, 25, 52) and the ncSP score was calculated using the ncSP calculator web server (53, 54).

NADase binding to OKP7 cells detected by flow cytometry. Primary immortalized human palate keratinocytes (OKP7, a gift from James Rheinwald) (55) were grown to near-confluence in a T75 plate in keratinocyte serum-free medium (KSFM) as previously described (15). For initial flow cytometry experiments (Fig. 1), cells were then lifted by treating with 1.5 ml 0.25% trypsin-EDTA at 37°C for 5 to 7 min. We then added DMEM plus 10% FBS and pelleted the cells. Cells were resuspended in KSFM and counted. They were then washed twice and 500,000 cells per well were added to a 96-well U-bottom plate preblocked with 2% albumin in PBS. Cells were again pelleted and resuspended in 200 μl PBS/1 mM DTT containing 3 μM toxins directly labeled with Alexa Fluor 488 as described above. Dye:protein molar ratios for each toxin were as

follows: NADase, 0.4; glycohydrolase domain (190 NADase), 1.04; NT194NADase, 0.72; and ovalbumin, 0.514. Cells were incubated at 37°C for 20 min then washed with 200 μl ice-cold PBS three times. They were then fixed with 2% paraformaldehyde (PFA) at RT for 15 min, washed with PBS, and transferred to flow cytometry tubes. We measured 10,000 intact cells for green fluorescence on a FACSCalibur (BD Biosciences) using standard protocols. Data from at least three independent experiments were visualized on FlowJo10.5.0 (FlowJo, LLC) and analyzed by ANOVA with Tukey's comparison in GraphPad Prism 9 (GraphPad Software, Inc.).

NADase binding to OKP7 cells detected by confocal fluorescence microscopy. To avoid possible detrimental effects of lifting cells with trypsin for toxin binding experiments, we additionally investigated toxin binding using confocal microscopy. OKP7 (55) cells were seeded on glass coverslips in 24-well plates and grown to near-confluence, (15) then washed with PBS three times. 300 μl of Alexa Fluor 488-labeled toxin at 1 μM concentrations in PBS/1 mM DTT were added to cells and incubated at room temperature for 30 min. Dye:protein molar ratios (R) were as follows: NADase, 1.15; glycohydrolase domain, 1.04; translocation domain, 0.72; IFS, 2.3. Cells were then washed three times with ice cold PBS and subsequently fixed with 4% PFA at room temperature for 15 min. They were then washed twice with PBS, treated with 0.1% Triton X-100 and stained with DAPI at 2 μM and Alexa Fluor 647-conjugated phalloidin (Thermo) at 13 μM. They were subsequently washed extensively with PBS/0.05% Tween 20 and then PBS and mounted with Prolong Gold (Thermo) on glass slides. Microscopy was completed on a Zeiss LSM880 inverted confocal microscope with Airyscan at the Harvard Digestive Diseases Center Core Facility. Images were processed with Zen imaging software (Zeiss). For binding quantitation, 2 $\times$ 2 tile scans were collected, and cells were counted (>100) by an observer blinded to treatment allocations. The number of cells with bound toxin are represented as a percentage of total. At least three independent experiments were completed, and the results were analyzed by ANOVA with Tukey's comparison in GraphPad Prism 9 (GraphPad Software, Inc.).

Calcium binding experiments. Calcium binding to the NADase translocation domain was studied both by calorimetry and by NMR spectroscopy. For calorimetry, protein was dialyzed twice in 1 L 20 mM Tris, 50 mM NaCl, 5 mM EDTA, 1 gm dry weight of Chelex and then twice with the same buffer but without EDTA. This was done to make every attempt at removing calcium. We then used a MicroCal ITC 200 at the Center for Macromolecular Interactions of Harvard Medical School with 420 μM protein in the cell and 20 mM $CaCl_2$ in the syringe at 30°C. The only effect we saw was from buffer dilution and visible in our negative buffer only control. There was no clear calcium binding effect.

For NMR spectroscopy experiments, ^{15}N-labeled NADaseNT194 was dialyzed into 20 mM MES, 50 mM NaCl, 10 mM $CaCl_2$, pH 5.5. A reference 2D ^{1}H-^{15}N TROSY-HSQC spectrum was then acquired at 600 MHz ^{1}H frequency. Protein concentration was 100 μM. We then dialyzed another NADaseNT194 sample over 2 days initially in 20 mM MES, 50 mM NaCl, 2 mM EDTA (pH 5.5), and 1 g Chelex 100 resin (Bio-Rad) and then twice in 20 mM MES, 50 mM NaCl, 1 mM EDTA (pH 5.5), and 1 g Chelex. A 2D ^{1}H^{15}N TROSY-HSQC spectrum of a sample with a final protein concentration of 225 μM was then recorded using exactly identical parameters as for the above sample containing 10 mM $CaCl_2$. Chemical shift perturbations and peak intensities were evaluated overlaying and comparing the two spectra in CARA. Garrett plot was calculated as previously described (56).

BLI. BLI experiments were performed in an Octet RED384 system (Sartorius).

Binding of biotinylated m-SLO with NADase and NADase variants was assayed as previously described for SLO and NADase (15). m-SLO was loaded onto streptavidin-coated sensor tips (Sartorius) at 50 nM concentrations. NADase and its variants were tested at 20 μM with subsequent 2-fold dilutions to 312.5 nM final concentration. Experimental parameters are as previously described (15). Buffer used throughout the experiments was 20 mM Tris, 300 mM NaCl, 1 mM DTT, 0.05% Tween 20, pH 7.4. Data were double subtracted with m-SLO negative and NADase/variant negative data. K_D was determined from response saturation curves of three independent experiments as previously described using Octet analysis software version 12.0 and GraphPad Prism 9.0.

Monomeric SLO keratinocyte binding inhibition assays. Purified m-SLO was labeled with Alexa Fluor 488 as described above. The resulting dye:protein molar ratio for m-SLO was 1.3. Binding assays were carried out with slight modifications as described above for NADase binding to OKP7s detected by flow cytometry. m-SLO concentrations in our assays were 20 nM in PBS, 1 mM DTT. When used in combination with NADase, NADase variants, or IFS as our negative control, the second protein species was added to the solution at 10 μM concentrations. Toxins were incubated with cells at 37°C, 20 min, then washed three times with ice cold PBS, fixed, and assayed by flow cytometry as described above. In this assay, any measured fluorescence is representative of m-SLO binding to OKP7s. Statistical analysis was completed in GraphPad Prism 9.0 by ANOVA with Tukey's comparison using data from at least three independent experiments.

Hemolysis inhibition assays. Hemolysis assays were modified from previously described standard hemolysis assays (57). Briefly, experiments were carried out in 96-well v-bottom plates. All conditions except our negative control (PBS, 1 mM DTT) contained a final SLO concentration of 0.5 nM in PBS, 1 mM DTT. NADase, IFS, and NADase variants were added to individual wells starting at 20 μM concentrations with subsequent 2-fold dilutions to 19.5 nM with a final volume per well of 300 μl. Thirty microliters of PBS-washed sheep defibrinated ertyhrocytes (Remel) were then added to all wells and incubated at 37°C for 10 min. The plate was centrifuged at 2,500 rpm, 10 min, 4°C. One hundred microliters of supernatant was transferred to an ELISA plate and absorbance was measured at a 550 nm wavelength. Average absorbance values for 4 negative control wells (PBS alone) were subtracted and data normalized to the average absorbance from hemolysis with 0.5 nM SLO in the absence of any additional proteins. Absorbance data were plotted versus concentration of NADase, NADase variants, or IFS and a hemolysis IC_{50} was determined from concentrations where only 50% hemolysis was achieved. Experiments were repeated at least 3 times and statistical significance was

determined by ANOVA with Tukey's comparison. All data analysis, graphical representation, and statistical analysis was completed with GraphPad Prism 9.0.

Circular dichroism (CD) spectroscopy. CD spectroscopy was carried out as previously described for full-length NADase (37) in a JASCO J-815 spectropolarimeter at the Center for Macromolecular Interactions of Harvard Medical School. NADase and its variants were dialyzed against 10 mM phosphate, 0.5 mM DTT, pH 8.0, and measured in a 10 mm stoppered quartz cuvette at 20°C using 0.5 nm steps from 190 to 260 nm and a 1 nm bandwidth. Protein concentration for all species was 4 μM. Five scans were collected, averaged and smoothed and a background only spectrum was subtracted. Data were analyzed using GraphPad Prism 9.0.

Dynamic light scattering. The hydrodynamic radius of NADase and NADase variants was measured by dynamic light scattering in a Malvern Zetasizer Nano ZS at protein concentrations of 1 mg/ml in PBS at 30°C. Reported hydrodynamic radius was for monodisperse peaks representing species greater than 99% abundance by mass.

Data availability. Atomic structure coordinates and structural constraints have been deposited in the Protein Data Bank (PDB) under accession number 7JI1. Chemical shift values have been deposited in the Biological Magnetic Resonance Data Bank (BMRB) under accession number 30779. Additional data that support the findings of this study will be supplied upon reasonable request.

SUPPLEMENTAL MATERIAL

Supplemental material is available online only.

SUPPLEMENTAL FILE 1, PDF file, 3.3 MB.

ACKNOWLEDGMENTS

We are grateful to Kelly Arnett and the Center for Macromolecular Interactions of the Harvard Medical School for help with CD spectroscopy, biolayer interferometry, and microcalorimetry. We are also thankful for helpful discussions regarding experimental design with multiple members of the Wessels and Chou laboratories.

This work was supported by grant K08-AI112823 to J.J.V. and by R01-AI130019 to M.R.W. from the NIAID (National Institutes of Health).

REFERENCES

1. Nasser W, Beres SB, Olsen RJ, Dean MA, Rice KA, Long SW, Kristinsson KG, Gottfredsson M, Vuopio J, Raisanen K, Caugant DA, Steinbakk M, Low DE, McGeer A, Darenberg J, Henriques-Normark B, Van Beneden CA, Hoffmann S, Musser JM. 2014. Evolutionary pathway to increased virulence and epidemic group A Streptococcus disease derived from 3,615 genome sequences. Proc Natl Acad Sci U S A 111:E1768–E1776. https://doi.org/10.1073/pnas.1403138111.
2. Zhu L, Olsen RJ, Nasser W, Beres SB, Vuopio J, Kristinsson KG, Gottfredsson M, Porter AR, DeLeo FR, Musser JM. 2015. A molecular trigger for intercontinental epidemics of group A Streptococcus. J Clin Invest 125:3545–3559. https://doi.org/10.1172/JCI82478.
3. Sumby P, Porcella SF, Madrigal AG, Barbian KD, Virtaneva K, Ricklefs SM, Sturdevant DE, Graham MR, Vuopio-Varkila J, Hoe NP, Musser JM. 2005. Evolutionary origin and emergence of a highly successful clone of serotype M1 group a Streptococcus involved multiple horizontal gene transfer events. J Infect Dis 192:771–782. https://doi.org/10.1086/432514.
4. Zhu L, Olsen RJ, Nasser W, de la Riva Morales I, Musser JM. 2015. Trading capsule for increased cytotoxin production: contribution to virulence of a newly emerged clade of emm89 *Streptococcus pyogenes*. mBio 6:e01378-15. https://doi.org/10.1128/mBio.01378-15.
5. Turner CE, Abbott J, Lamagni T, Holden MT, David S, Jones MD, Game L, Efstratiou A, Sriskandan S. 2015. Emergence of a new highly successful acapsular group A streptococcus clade of genotype emm89 in the United Kingdom. mBio 6:e00622. https://doi.org/10.1128/mBio.00622-15.
6. Zhu L, Olsen RJ, Lee JD, Porter AR, DeLeo FR, Musser JM. 2017. Contribution of secreted NADase and streptolysin O to the pathogenesis of epidemic serotype M1 *Streptococcus pyogenes* infections. Am J Pathol 187:605–613. https://doi.org/10.1016/j.ajpath.2016.11.003.
7. Tweten RK, Hotze EM, Wade KR. 2015. The unique molecular choreography of giant pore formation by the cholesterol-dependent cytolysins of gram-positive bacteria. Annu Rev Microbiol 69:323–340. https://doi.org/10.1146/annurev-micro-091014-104233.
8. Tweten RK, Parker MW, Johnson AE. 2001. The cholesterol-dependent cytolysins. Curr Top Microbiol Immunol 257:15–33. https://doi.org/10.1007/978-3-642-56508-3_2.
9. Chandrasekaran S, Caparon MG. 2015. The *Streptococcus pyogenes* NAD(+) glycohydrolase modulates epithelial cell PARylation and HMGB1 release. Cell Microbiol 17:1376–1390. https://doi.org/10.1111/cmi.12442.
10. Chandrasekaran S, Caparon MG. 2016. The NADase-negative variant of the *Streptococcus pyogenes* toxin NAD(+) glycohydrolase induces JNK1-mediated programmed cellular necrosis. mBio 7:e02215-15. https://doi.org/10.1128/mBio.02215-15.
11. Ghosh J, Anderson PJ, Chandrasekaran S, Caparon MG. 2010. Characterization of *Streptococcus pyogenes* beta-NAD+ glycohydrolase: re-evaluation of enzymatic properties associated with pathogenesis. J Biol Chem 285:5683–5694. https://doi.org/10.1074/jbc.M109.070300.
12. Bricker AL, Cywes C, Ashbaugh CD, Wessels MR. 2002. NAD+-glycohydrolase acts as an intracellular toxin to enhance the extracellular survival of group A streptococci. Mol Microbiol 44:257–269. https://doi.org/10.1046/j.1365-2958.2002.02876.x.
13. Bastiat-Sempe B, Love JF, Lomayesva N, Wessels MR. 2014. Streptolysin O and NAD-glycohydrolase prevent phagolysosome acidification and promote group A Streptococcus survival in macrophages. mBio 5:e01690-14. https://doi.org/10.1128/mBio.01690-14.
14. O'Seaghdha M, Wessels MR. 2013. Streptolysin O and its co-toxin NAD-glycohydrolase protect group A Streptococcus from Xenophagic killing. PLoS Pathog 9:e1003394. https://doi.org/10.1371/journal.ppat.1003394.
15. Velarde JJ, O'Seaghdha M, Baddal B, Bastiat-Sempe B, Wessels MR. 2017. Binding of NAD+-glycohydrolase to streptolysin O stabilizes both toxins and promotes virulence of group A streptococcus. mBio 8:e01382-17. https://doi.org/10.1128/mBio.01382-17.
16. Madden JC, Ruiz N, Caparon M. 2001. Cytolysin-mediated translocation (CMT): A functional equivalent of type III secretion in gram-positive bacteria. Cell 104:143–152. https://doi.org/10.1016/s0092-8674(01)00198-2.
17. Magassa N, Chandrasekaran S, Caparon MG. 2010. *Streptococcus pyogenes* cytolysin-mediated translocation does not require pore formation by streptolysin O. EMBO Rep 11:400–405. https://doi.org/10.1038/embor.2010.37.
18. Ghosh J, Caparon MG. 2006. Specificity of *Streptococcus pyogenes* NAD(+) glycohydrolase in cytolysin-mediated translocation. Mol Microbiol 62:1203–1214. https://doi.org/10.1111/j.1365-2958.2006.05430.x.

19. Yoon JY, An DR, Yoon HJ, Kim HS, Lee SJ, Im HN, Jang JY, Suh SW. 2013. High-resolution crystal structure of *Streptococcus pyogenes* beta-NAD(+) glycohydrolase in complex with its endogenous inhibitor IFS reveals a highly water-rich interface. J Synchrotron Radiat 20:962–967. https://doi.org/10.1107/S0909049513020803.
20. Smith CL, Ghosh J, Elam JS, Pinkner JS, Hultgren SJ, Caparon MG, Ellenberger T. 2011. Structural basis of *Streptococcus pyogenes* immunity to its NAD+ glycohydrolase toxin. Structure 19:192–202. https://doi.org/10.1016/j.str.2010.12.013.
21. Mozola CC, Caparon MG. 2015. Dual modes of membrane binding direct pore formation by streptolysin O. Mol Microbiol 97:1036–1050. https://doi.org/10.1111/mmi.13085.
22. Mozola CC, Magassa N, Caparon MG. 2014. A novel cholesterol-insensitive mode of membrane binding promotes cytolysin-mediated translocation by streptolysin O. Mol Microbiol 94:675–687. https://doi.org/10.1111/mmi.12786.
23. Gibbs EB, Cook EC, Showalter SA. 2017. Application of NMR to studies of intrinsically disordered proteins. Arch Biochem Biophys 628:57–70. https://doi.org/10.1016/j.abb.2017.05.008.
24. Shen Y, Delaglio F, Cornilescu G, Bax A. 2009. TALOS+: a hybrid method for predicting protein backbone torsion angles from NMR chemical shifts. J Biomol NMR 44:213–223. https://doi.org/10.1007/s10858-009-9333-z.
25. Berjanskii MV, Wishart DS. 2005. A simple method to predict protein flexibility using secondary chemical shifts. J Am Chem Soc 127:14970–14971. https://doi.org/10.1021/ja054842f.
26. Holm L. 2020. DALI and the persistence of protein shape. Protein Sci 29:128–140. https://doi.org/10.1002/pro.3749.
27. Abbott DW, Boraston A. 2011. Structural analysis of a putative family 32 carbohydrate-binding module from the *Streptococcus pneumoniae* enzyme EndoD. Acta Crystallogr Sect F Struct Biol Cryst Commun 67:429–433. https://doi.org/10.1107/S1744309111001874.
28. Grondin JM, Duan D, Kirlin AC, Abe KT, Chitayat S, Spencer HL, Spencer C, Campigotto A, Houliston S, Arrowsmith CH, Allingham JS, Boraston AB, Smith SP. 2017. Diverse modes of galacto-specific carbohydrate recognition by a family 31 glycoside hydrolase from *Clostridium perfringens*. PLoS One 12:e0171606. https://doi.org/10.1371/journal.pone.0171606.
29. Feil SC, Lawrence S, Mulhern TD, Holien JK, Hotze EM, Farrand S, Tweten RK, Parker MW. 2012. Structure of the lectin regulatory domain of the cholesterol-dependent cytolysin lectinolysin reveals the basis for its lewis antigen specificity. Structure 20:248–258. https://doi.org/10.1016/j.str.2011.11.017.
30. Armenta S, Moreno-Mendieta S, Sanchez-Cuapio Z, Sanchez S, Rodriguez-Sanoja R. 2017. Advances in molecular engineering of carbohydrate-binding modules. Proteins 85:1602–1617. https://doi.org/10.1002/prot.25327.
31. Shewell LK, Harvey RM, Higgins MA, Day CJ, Hartley-Tassell LE, Chen AY, Gillen CM, James DB, Alonzo F, 3rd, Torres VJ, Walker MJ, Paton AW, Paton JC, Jennings MP. 2014. The cholesterol-dependent cytolysins pneumolysin and streptolysin O require binding to red blood cell glycans for hemolytic activity. Proc Natl Acad Sci U S A 111:E5312–20. https://doi.org/10.1073/pnas.1412703111.
32. Farrand S, Hotze E, Friese P, Hollingshead SK, Smith DF, Cummings RD, Dale GL, Tweten RK. 2008. Characterization of a streptococcal cholesterol-dependent cytolysin with a lewis y and b specific lectin domain. Biochemistry 47:7097–7107. https://doi.org/10.1021/bi8005835.
33. Shewell LK, Day CJ, Jen FE, Haselhorst T, Atack JM, Reijneveld JF, Everest-Dass A, James DBA, Boguslawski KM, Brouwer S, Gillen CM, Luo Z, Kobe B, Nizet V, von Itzstein M, Walker MJ, Paton AW, Paton JC, Torres VJ, Jennings MP. 2020. All major cholesterol-dependent cytolysins use glycans as cellular receptors. Sci Adv 6:eaaz4926. https://doi.org/10.1126/sciadv.aaz4926.
34. Xu C, Gagnon E, Call ME, Schnell JR, Schwieters CD, Carman CV, Chou JJ, Wucherpfennig KW. 2008. Regulation of T cell receptor activation by dynamic membrane binding of the CD3epsilon cytoplasmic tyrosine-based motif. Cell 135:702–713. https://doi.org/10.1016/j.cell.2008.09.044.
35. Zitzer A, Bittman R, Verbicky CA, Erukulla RK, Bhakdi S, Weis S, Valeva A, Palmer M. 2001. Coupling of cholesterol and cone-shaped lipids in bilayers augments membrane permeabilization by the cholesterol-specific toxins streptolysin O and *Vibrio cholerae* cytolysin. J Biol Chem 276:14628–14633. https://doi.org/10.1074/jbc.M100241200.
36. Morton CJ, Sani MA, Parker MW, Separovic F. 2019. Cholesterol-dependent cytolysins: Membrane and protein structural requirements for pore formation. Chem Rev 119:7721–7736. https://doi.org/10.1021/acs.chemrev.9b00090.
37. Sharma O, O'Seaghdha M, Velarde JJ, Wessels MR. 2016. NAD+-glycohydrolase promotes intracellular survival of group A streptococcus. PLoS Pathog 12:e1005468. https://doi.org/10.1371/journal.ppat.1005468.
38. Kay LE, Ikura M, Tschudin R, Bax A. 2011. Three-dimensional triple-resonance NMR Spectroscopy of isotopically enriched proteins. 1990. J Magn Reson 213:423–441. https://doi.org/10.1016/j.jmr.2011.09.004.
39. Salzmann M, Wider G, Pervushin K, Senn H, Wüthrich K. 1999. TROSY-type triple-resonance experiments for sequential NMR assignments of large proteins. J Am Chem Soc 121:844–848. https://doi.org/10.1021/ja9834226.
40. Delaglio F, Grzesiek S, Vuister GW, Zhu G, Pfeifer J, Bax A. 1995. NMRPipe: a multidimensional spectral processing system based on UNIX pipes. J Biomol NMR 6:277–293. https://doi.org/10.1007/BF00197809.
41. Keller R. 2004. The computer aided resonance assignment tutorial. CANTINA, Verlag, Germany.
42. Bartels C, Xia TH, Billeter M, Guntert P, Wuthrich K. 1995. The program XEASY for computer-supported NMR spectral analysis of biological macromolecules. J Biomol NMR 6:1–10. https://doi.org/10.1007/BF00417486.
43. Schwieters CD, Kuszewski JJ, Tjandra N, Clore GM. 2003. The Xplor-NIH NMR molecular structure determination package. J Magn Reson 160:65–73. https://doi.org/10.1016/s1090-7807(02)00014-9.
44. Chen VB, Arendall WB, 3rd, Headd JJ, Keedy DA, Immormino RM, Kapral GJ, Murray LW, Richardson JS, Richardson DC. 2010. MolProbity: all-atom structure validation for macromolecular crystallography. Acta Crystallogr D Biol Crystallogr 66:12–21. https://doi.org/10.1107/S0907444909042073.
45. Laskowski RA, Rullmannn JA, MacArthur MW, Kaptein R, Thornton JM. 1996. AQUA and PROCHECK-NMR: programs for checking the quality of protein structures solved by NMR. J Biomol NMR 8:477–486. https://doi.org/10.1007/BF00228148.
46. The PyMOL Molecular Graphics System, version 2.3.2.Schrödinger, LLC.
47. Pettersen EF, Goddard TD, Huang CC, Couch GS, Greenblatt DM, Meng EC, Ferrin TE. 2004. UCSF Chimera—a visualization system for exploratory research and analysis. J Comput Chem 25:1605–1612. https://doi.org/10.1002/jcc.20084.
48. Sarkar S, Witham S, Zhang J, Zhenirovskyy M, Rocchia W, Alexov E. 2013. DelPhi Web Server: A comprehensive online suite for electrostatic calculations of biological macromolecules and their complexes. Commun Comput Phys 13:269–284. https://doi.org/10.4208/cicp.300611.201011s.
49. Smith N, Witham S, Sarkar S, Zhang J, Li L, Li C, Alexov E. 2012. DelPhi web server v2: incorporating atomic-style geometrical figures into the computational protocol. Bioinformatics 28:1655–1657. https://doi.org/10.1093/bioinformatics/bts200.
50. Holm L. 2019. Benchmarking Fold Detection by DaliLite v.5. Bioinformatics 35:5326–5327. https://doi.org/10.1093/bioinformatics/btz536.
51. Stivala A, Wybrow M, Wirth A, Whisstock JC, Stuckey PJ. 2011. Automatic generation of protein structure cartoons with Pro-origami. Bioinformatics 27:3315–3316. https://doi.org/10.1093/bioinformatics/btr575.
52. Shen Y, Bax A. 2015. Protein structural information derived from NMR chemical shift with the neural network program TALOS-N. Methods Mol Biol 1260:17–32. https://doi.org/10.1007/978-1-4939-2239-0_2.
53. Tamiola K, Acar B, Mulder FA. 2010. Sequence-specific random coil chemical shifts of intrinsically disordered proteins. J Am Chem Soc 132:18000–18003. https://doi.org/10.1021/ja105656t.
54. Tamiola K, Mulder FA. 2012. Using NMR chemical shifts to calculate the propensity for structural order and disorder in proteins. Biochem Soc Trans 40:1014–1020. https://doi.org/10.1042/BST20120171.
55. Dickson MA, Hahn WC, Ino Y, Ronfard V, Wu JY, Weinberg RA, Louis DN, Li FP, Rheinwald JG. 2000. Human keratinocytes that express hTERT and also bypass a p16(INK4a)-enforced mechanism that limits life span become immortal yet retain normal growth and differentiation characteristics. Mol Cell Biol 20:1436–1447. https://doi.org/10.1128/MCB.20.4.1436-1447.2000.
56. Garrett DS, Seok YJ, Peterkofsky A, Clore GM, Gronenborn AM. 1997. Identification by NMR of the binding surface for the histidine-containing phosphocarrier protein HPr on the N-terminal domain of enzyme I of the *Escherichia coli* phosphotransferase system. Biochemistry (Mosc) 36:4393–4398. https://doi.org/10.1021/bi970221q.
57. Ruiz N, Wang B, Pentland A, Caparon M. 1998. Streptolysin O and adherence synergistically modulate proinflammatory responses of keratinocytes to group A streptococci. Mol Microbiol 27:337–346. https://doi.org/10.1046/j.1365-2958.1998.00681.x.